Chemical Engineering Science 267 (2023) 118349

Contents lists available at ScienceDirect

Chemical Engineering Science

journal homepage: www.elsevier.com/locate/ces

Flow dynamics and mixing past pairs of confined microfluidic cylinders

Shigang Zhang [a,b], Yuang Han [a], Tom Lacassagne [b,c], Neil Cagney [b,d], Carolina P. Naveira-Cotta [e], Stavroula Balabani [b,f,*], Manish K. Tiwari [a,f,*]

[a] Nanoengineered Systems Laboratory, Department of Mechanical Engineering, University College London (UCL), London WC1E 7JE, UK
[b] FluME, Department of Mechanical Engineering, University College London (UCL), London WC1E 7JE, UK
[c] IMT Nord Europe, Institut Mines-Télécom, Univ. Lille, Centre for Energy and Environment, F-59000 Lille, France
[d] School of Engineering and Materials Science, Queen Mary University of London, London, UK
[e] Mechanical Engineering Department (PEM), Federal University of Rio de Janeiro-UFRJ, Rio de Janeiro, RJ, Brazil
[f] Wellcome/EPSRC Centre for Interventional and Surgical Sciences, University College London (UCL), London, UK

HIGHLIGHTS

- Mixing induced by pairs of microfluidic cylinders is investigated experimentally.
- Micro Particle Image Velocimetry (μPIV) and micro Laser Induced Fluorescence (μPLIF) are employed.
- Steady and unsteady flow regimes and various arrangements (tandem, staggered) are explored.
- Mixing enhancement is found to depend strongly on cylinder arrangement and flow regime.
- Staggered arrays perform better at low Reynolds number while tandem ones under conditions of vortex-shedding.

ARTICLE INFO

Article history:
Received 16 September 2022
Received in revised form 4 November 2022
Accepted 21 November 2022
Available online 25 November 2022

Keywords:
Fluid mechanics
Micromixing
Tandem arrangement
Staggered arrangement
Micro laser-induced fluorescence (μLIF)
Micro particle image velocimetry (μPIV)

ABSTRACT

Placing cylindrical obstacles in a micromixer is a promising means to enhance mass transport. However, there is still a lack of fundamental understanding on the effect of obstacle arrangement on the flow. The present work provides new experimental insights into confined inertia flows past two cylindrical pins, placed either in tandem or staggered arrangement in a Y-type micromixer, and their effect on mixing, through micro Particle Image Velocimetry (μPIV) and Laser Induced Fluorescence (μLIF) measurements. It is found that in such confined microfluidic environments, adding a second pin suppresses vortex-shedding for spacings less than 3.5-pin diameters in a tandem arrangement or 0.25-pin diameters in the staggered configurations. Vortex-shedding is found to enhance mixing in tandem configurations but not in staggered ones. The results highlight the important roles of both pin arrangement and flow instabilities in micromixer performance and can serve as a guide to micromixer design.

1. Introduction

The flow past cylinders is a canonical problem in fluid mechanics. The case of single or pairs of cylinders in unconfined flows has been widely studied experimentally (Cantwell and Coles, 1983; Sumner et al., 2000) and numerically (Chen et al., 2020; Griffith et al., 2017). This flow configuration has attracted great interest in the context of passive micromixers. In such small length scales and diffusion-dominated laminar flows, mixing is inherently challenging. (Lee et al., 2016; Yang et al., 2015). Placing cylindrical obstacles in the fluid path provides a promising route to enhance mixing, heat and mass transfer, and has thus attracted great interest in a range of applications, including particle dispersion (Bhagat and Papautsky, 2008), biodiesel synthesis (Costa Junior et al., 2020; Santana et al., 2019) and electronics cooling (Renfer et al., 2011).

In microfluidic channels, the flow past cylinders typically experiences some unique characteristics associated with the high blockage (defined as the ratio of cylinder diameter to channel width) and low aspect ratios (cylinder length to diameter ratio) (Renfer et al., 2013) arising from the dimensions of microfluidic devices, typically in the sub-millimetre range (Chen et al., 2009). The latter suppress vortex-shedding as found in our previous study (Zhang et al., 2019). Computational (Griffith et al., 2011; Kanaris et al., 2011; Mathupriya et al., 2018) and experimental studies (Jung et al., 2012; Zhang et al., 2020) have shown evidence of

* Corresponding authors at: Wellcome/EPSRC Centre for Interventional and Surgical Sciences, University College London (UCL), London, UK.
E-mail addresses: s.balabani@ucl.ac.uk (S. Balabani), m.tiwari@ucl.ac.uk (M.K. Tiwari).

https://doi.org/10.1016/j.ces.2022.118349
0009-2509/

vortex-shedding at sufficiently high Reynolds number ($Re = U_oD/\nu$, where U_o is the average velocity of the flow upstream of the pin, D is the cylinder diameter and ν is the kinematic viscosity of the fluid), resulting in more efficient mixing performance, especially when the centre of the pin and the interface between the two flow streams are aligned (Zhang et al., 2020).

However, the combined effects of confinement and multiple pin arrangements on the onset of vortex-shedding and flow unsteadiness, which could be harnessed to further enhance or control mixing processes in such micromixers, remain fairly unexplored. The literature on multiple micropin based micromixers has concentrated on complex configurations and relatively low Reynolds numbers ($Re < 100$). For example, Bhagat et al. (2007) investigated the flow in arrays of micropins with different heights, obstacle shapes and configurations. The most effective mixing was observed when the obstacles spanned the full microchannel height and had a diamond-shaped cross-section (compared to triangular and circular pins). The effect of obstacle shape was numerically investigated by Tata Rao et al. (2019); circle, diamond, ellipse, and triangle shaped pins were studied, and circle and diamond-shaped ones were found to provide the best mixing performance ($1 < Re < 100$). Micropin micromixers have been optimized by modifying the shape of channel walls (Wu et al., 2014) or using non-Newtonian fluids (Zhao et al., 2016). In these low Re number studies the enhanced mixing performance arises from the increased interfacial area induced by the obstructions or fluid elasticity rather than flow unsteadiness induced by vortex-shedding. Numerical simulations of higher Re flows (Re = 6–700) in a micromixer with circular pin arrays in tandem have shown a monotonic increase of the mixing index at high Re (Dundi et al., 2019). This could be due to vortex-shedding but no relevant information was provided.

The flow past two circular cylinders depends primarily on their arrangement and has been described in detail in many seminal works (Sumner, 2010; Zdravkovich, 1977) for long unconfined cylinders, serving as a useful starting point to study micropin flows. Various arrangements arise by varying the distance between the pins (pitch ratio) and the angle of incidence. The tandem arrangement, in which one cylinder is behind the other, and the staggered one, in which the cylinders are offset from one another in the transverse direction, are very common. The tandem arrangement can be described only by the longitudinal pitch ratio (L/D), i.e. the ratio of centre-to-centre longitudinal spacing (L) to pin diameter (see Fig. 1). For small longitudinal pitch ratios ($L/D < 2$), an 'extended-body' flow regime has been identified in which the two cylinders behave as a single bluff body (Zhou and Yiu, 2006). When L/D increases above 2 and up to a critical value (around 3.6) (Hosseini et al., 2021), flow enters the so called 'reattachment' regime in which the front cylinder separating shear layers reattach onto the one downstream; the downstream cylinder may act as a wake-stabilizer, in this case suppressing the onset of vortex-shedding. When L/D exceeds the critical value, vortex-shedding occurs from both cylinders and a 'co-shedding' regime establishes. In particular, the vortices from the first cylinder impinge on the downstream one creating a two-row vortex structure which has been recently found to possess a unique ability to either cloak or broadcast a third body placed downstream (Hosseini et al., 2021).

The more general case of staggered arrangements can be described using two geometrical parameters; the longitudinal and the transverse pitch ratios, L/D and T/D respectively. Various flow patterns as a function of L/D and T/D have been identified by Sumner (2010) for two unconfined cylinders in staggered arrangement and Re = 850 to 1900; these include shear layer reattachment (SLR), induced separation (IS), synchronized vortex-shedding (SVS) and vortex impingement (VI). The critical pitch ratios for the above regimes have been found to be weakly affected by Re for a wide range ($200 < Re < 10^5$) (Sumner, 2010).

The flow past a pair of cylinders continues to attract great interest in a range of applications across the scales, including noise control from the aircraft landing gear (Geyer, 2022), moisture removal (Zheng et al., 2021), heat transfer enhancement (Li et al., 2022), to name but a few. However, it is not well known how confinement such as that encountered in microfluidics affects the flow regimes and transitions previously reported, in particular the critical Re for onset of vortex-shedding. Most experimental studies have dealt with unconfined channels and higher than critical Re (Igarashi, 1981; Ishigai et al., 1972; Tasaka et al., 2006; Xu and Zhou, 2004). Literature suggests (Mizushima and Suehiro, 2005) that tandem cylinders exhibit a higher critical Re for small spacings (L/D = 2) compared to single cylinders which progressively decreases, approaching that of a single cylinder for L/D values over 4 diameters. The critical Re is an important parameter for microfluidic mixing induced by micropins, as wake unsteadiness can lead to more efficient mixing (Zhang et al., 2020). A recent study by (Li et al., 2022) has numerically demonstrated the significant impact vortex shedding from two side by side freely rotating square cylinders can have on the heat transfer and mixing in a microchannel. The importance of confinement on vortex-shedding and micromixing was recently illustrated by Zhang et al. (2020, 2019) who investigated flow and mixing characteristics of a single micropin confined in both axial and lateral directions. Nonetheless, to the best of the authors' knowledge, the flow induced by two cylindrical micropins has not been rigorously studied, despite its numerous applications in microfluidics and microscale mixing. Vortex interactions are expected to have a strong influence on momentum and mass transfer; combined with the multitude of configurations they provide a

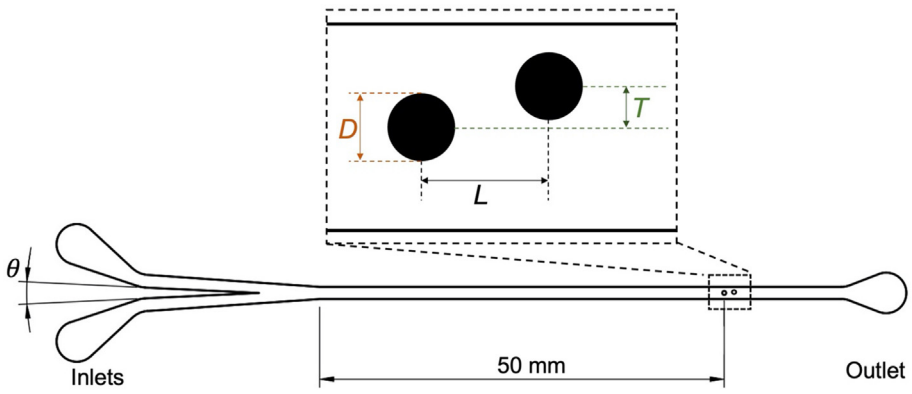

Fig.1. Schematic of a two pin microfluidic channel, showing the inlet angle (θ) and the definitions of the longitudinal and transverse pitch ratios (L/D and T/D).

route to control and optimise microscale processes -as illustrated in (Antognoli et al., 2021) and merit further investigation; hence the motivation for the present study.

In order to explore the influence of confinement and cylinder configurations on the wake dynamics and mixing performance of micromixers, we present instantaneous μPIV/ LIF measurements of microchannel flows containing pairs of pins in various tandem and staggered arrangements over a range of Re (up to 340). Additionally, a high-speed μPIV system is used to resolve the unsteady wake dynamics and shedding frequencies, and the intensity of segregation technique is applied to the μLIF measurements to quantify the mixing enhancement.

2. Experimental setup

2.1. Microfluidic chip fabrication

A CNC micro-milling machine (Minitech Machinery, Georgia) was used to fabricate the rectangular polymethyl methacrylate (PMMA) microchannels. As shown in Fig. 1, several channels with two cylindrical pins in different arrangements and a Y-junction inlet were bonded employing a solvothermal technique (Bamshad et al., 2016). The cylinder diameter was D = 500 ± 10 μm, the channel width W = 1500 ± 20 μm and the height H = 1000 ± 20 μm, resulting in a lateral confinement of W/D = 3 and a vertical one of H/D = 2. For the microchannels with two pins in tandem (T/D = 0), the centre-to-centre longitudinal spacing ranged from 1250 to 3250 μm (±30 μm) resulting in pitch ratios L/D in the range of 2.5–6.5, with both micropins located on the channel centreline. In microchannels with two pins in a staggered arrangement, the first cylindrical pin was located at the microchannel centreline and the second pin was offset at various distances from the centreline to obtain T/D values ranging from 0.25 to 0.75 with L/D remaining fixed at 2.5. Due to the confinement the range of transverse spacings range is in practice limited to T/D < 1 as the latter corresponds to the downstream cylinder touching the sidewall.

To minimize flow separation effects, the angle (θ, see Fig. 1) between the two inlet channels was kept small (6 ± 1°) to ensure a fully developed flow and no influence on the measured mixing enhancement (Hsieh et al., 2013; Soleymani et al., 2008). The first pin was located at 50 mm from inlet, i.e. 100 D; this was found sufficient to obtain fully developed flow.

2.2. Micro particle-image velocimetry (μPIV) system

Fig. 2 shows a schematic of the μPIV set up, described in detail in Zhang et al. (2020). Distilled water at room temperature was used as working fluid. The flow was seeded with 1 μm fluorescent particles (Nile Red) (ThermoFisher, UK) and delivered using a syringe pump (Harvard Bioscience, USA). The flowrate was varied between 0.2 and 105 ml/min (1 % uncertainty). A pulsed Nd-YAG laser (532 nm wavelength) (Litron Laser, UK) illuminated the flow and images were acquired at multiple planes using a scientific Complementary Metal-Oxide-Semiconductor (sCMOS) camera (Zyla 5.5, Andor, UK) and a 5 × microscope objective (NA = 0.14). 100 image-pairs (time interval between two pulses of 10 μs) 2560 × 2160 pixels^2 in size were acquired in each experiment with a framerate of 15 Hz. PIV processing was performed in Insight4G (TSI, USA); cross correlation with a starting interrogation window of 128 × 128 pixels^2, a final one of 64 × 64 pixels^2 and 50 % window overlap was implemented leading to a spatial resolution of 32 vectors per channel.

The origin of the coordinate system is located on the axis and midspan of the first pin. The x, y, and z axes denote the streamwise (flow), transverse and spanwise directions, respectively. Measurements were performed over the region x/D = -4 to 10, in order to characterise both the upstream flow and the far wake. This was larger than what could be covered in a single image pair, and therefore the measurements were performed in four separate overlapping segments. These segments could then be stitched together to produce composite fields. In the case of some statistical properties (mean velocity and root-mean-square) this composition is straightforward. It is more complicated for instantaneous measurements as it is necessary to ensure that each segment in a composite field corresponds to the same phase in the shedding cycle. Measurement in each separate field being performed asynchronously, composite fields for the instantaneous data were not strictly speaking full frame instantaneous fields but rather reconstruction of phase representative signals, and were used simply to provide a visual representation of the wake dynamics. They could be found by simply identifying segments that were at the same phase by visual inspection.

The measurements spanned the Re range from 39 to 340 (based on the pin diameter). The corresponding Re based on microchannel hydraulic diameter ranged from 78 to 680, i.e. flow is laminar. The velocity measurements are normalized by the average velocity U_o to facilitate comparisons and mitigate for errors arising from the depth of correlation. The latter is equal to 120 μm in the present set up (Olsen and Adrian, 2000). No velocity correction as suggested by Poelma et al. (2012) was therefore needed.

2.3. Micro laser-induced fluorescence (μLIF) system

μLIF measurements were conducted with the same set up using Rhodamine 6G (Sigma-Aldrich, UK) as a fluorescent dye (scalar) due to its well documented low temperature or pH sensitivity (Dusting and Balabani, 2009). The calibration procedures are detailed in the Supplementary Material S1. μLIF measurements were performed in a number of overlapping segments and stitched together to form larger composite fields as with μPIV.

The degree of mixing can be quantified using various metrics. The bulk or cup mixing average mass fraction method has been utilised by some groups (Aubin et al., 2010; Galletti et al., 2019) in which the degree of mixing on a specific cross-section is calculated from the variance of a flow weighted concentration σ (Mariotti et al., 2019):

$$M = 1 - \frac{\sigma}{\sigma_{max}} \tag{2}$$

with σ_{max} being the maximum value of σ, obtained when the two streams to be mixed remain completely segregated. A similar index, based on the intensity of segregation (I) is applied on the instantaneous concentration fields measured by μLIF in the present study to quantify mixing (Hoffmann et al., 2006; Wang et al., 2012; Zhang et al., 2020), defined as follows:

$$M = 1 - \sqrt{I} = 1 - \sqrt{\frac{{\sigma_c}^2}{\bar{C}(1-\bar{C})}} \tag{3}$$

where σ_c and $\bar{C}$ respectively are the standard deviation and mean of the normalized measured concentration over a given region. M = 1 indicates a perfectly mixed (homogeneous) fluid, and M = 0 a completely segregated one. M values at each location were then averaged over 100 instantaneous images, which was deemed sufficient for statistical convergence (unsteady flows were assumed statistically steady). The standard deviation for M over those 100 fields was used as an estimate of the uncertainty on M. Detailed validations are shown in the Supplementary Material

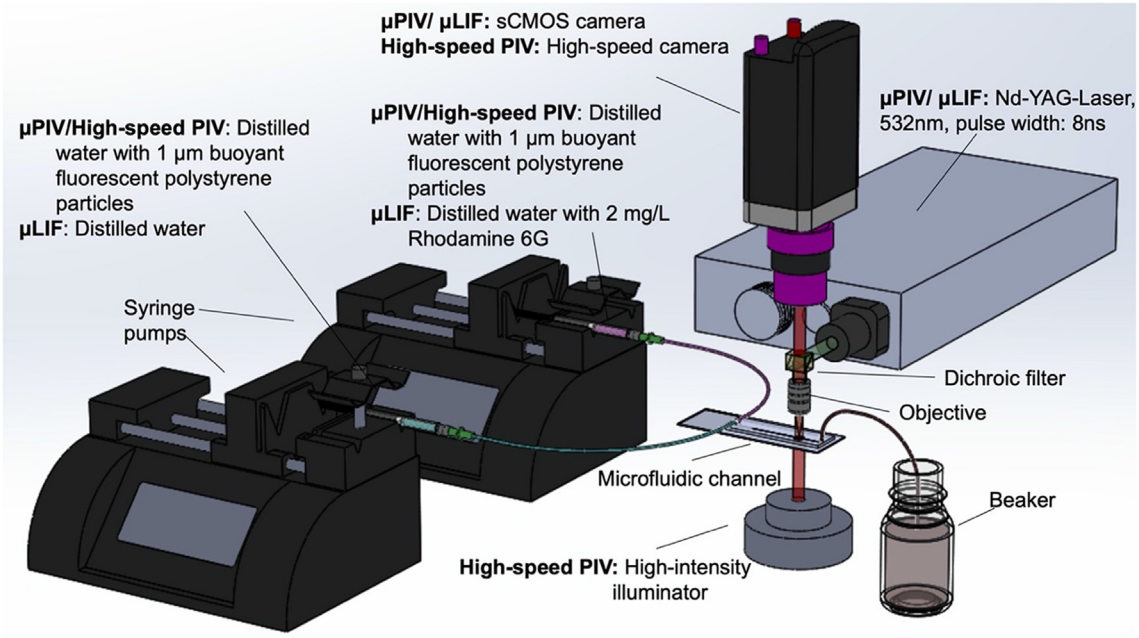

Fig. 2. Schematic of the μPIV and μLIF setup and the high-speed μPIV measurements.

S2. The reported M values are based on mid-plane (z/D = 0) concentration measurements, considered indicative of the mixing in a specific cross- sectional channel area (i.e. x/D).

2.4. High-speed μPIV system

In microfluidic channels, the frequency of vortex-shedding - when present - is too high (typically in the hundreds Hz range) for conventional μPIV systems to resolve. High-speed μPIV measurements were performed using brightfield illumination (150 W, Thorlabs, UK) and a high-speed camera (Phantom V411, USA). These allowed to temporally resolve the flow for Re up to 260, enabling us to capture the vortex-shedding frequency. Validation of the high-speed μPIV was demonstrated in our previous published work (Zhang et al., 2019). In each experiment, 9,000 images with a maximum size of 320 × 256 pixels, were acquired at a frame rate of 36 kHz. Multipass cross correlation was used with a starting interrogation window of 64 × 64 pixels^2 and a final one of 32 × 32 pixels^2; the spatial resolution was 4.3 μm/pixel.

2.5. Measurement errors

Based on the difference between the dominant and secondary peak in the PIV cross-correlation process (Pothos et al., 2016), the uncertainty in the PIV measurements was found to be around 2 %. The uncertainty on concentration measurements by the LIF method is about 2 %. The microchannel dimensions have an uncertainty of around 1 %. Moreover, the uncertainty in viscosity is around 4 % due to room temperature fluctuations. Therefore, the error in Re is estimated around 5 % in the present study by the error propagation formula.

3. Results and discussion

3.1. Upstream flow conditions

The flow approaching the first pin was examined at selected experimental conditions to verify that it is fully developed. Fig. 3 compares the experimental velocity profiles with the analytical solution (Aparecido and Cotta, 1990) and shows excellent agreement (within 2 %). The results thus confirm that the flow upstream of the first cylindrical pin is fully developed.

3.2. Wake and interface dynamics for tandem cylinders

Selected instantaneous out-of-plane vorticity fields (ω_z) in tandem flow configurations are shown in Fig. 4 for Re around 150, and L/D ranging from 2.5 to 6.5. A standard first order, forward finite difference approach (Wetton, 1992) was used to derive the velocity gradients required to calculate the vorticity fields. Note that the vorticity fields shown are stitched together from measurements at four flow regions, as explained in Section 2.2. Selected vorticity contours, streamlines and concentration fields at different Re are shown in the Supplementary Video 1.

In the microchannel with L/D = 2.5 (top row of Fig. 4), the shear layers from the first pin reattach onto the second one. Downstream of the second cylinder, the shear layers gradually converge near the wake centreline (y/D = 0) instead of rolling up to form vortices. The presence of the shear layers generates opposite signed vorticity between the layers and the neighbouring walls. While there is always some positive vorticity at the upper wall and negative vorticity at the lower wall associated with the boundary layers, the magnitude of vorticity in these regions increases significantly when the shear layers from the cylinder form, reaching a peak magnitude at x/D ≈ 6. Beyond this point all four shear layers have approximately equal magnitude vorticity.

For L/D = 4.5 (middle row of Fig. 4), the shear layers from the first pin begin to form into vortices and the waviness introduced propagates downstream to the wake of the second pin, resulting in clear shedding in its near-wake. This appears to induce roll up in the wall shear layers at x/D ≈ 7 (bottom wall) and ≈ 9 (top wall). When L/D is increased further (bottom row of Fig. 4), there is less unsteadiness in the wake. The shear layers from the first cylinder extend far into the wake, only beginning to roll up shortly before the second cylinder, while no vortex formation is seen behind the second cylinder. The non-monotonic effect of L/D on the appearance of vortex-shedding and the interaction between the shear layers formed at the wall and those formed at the cylinder

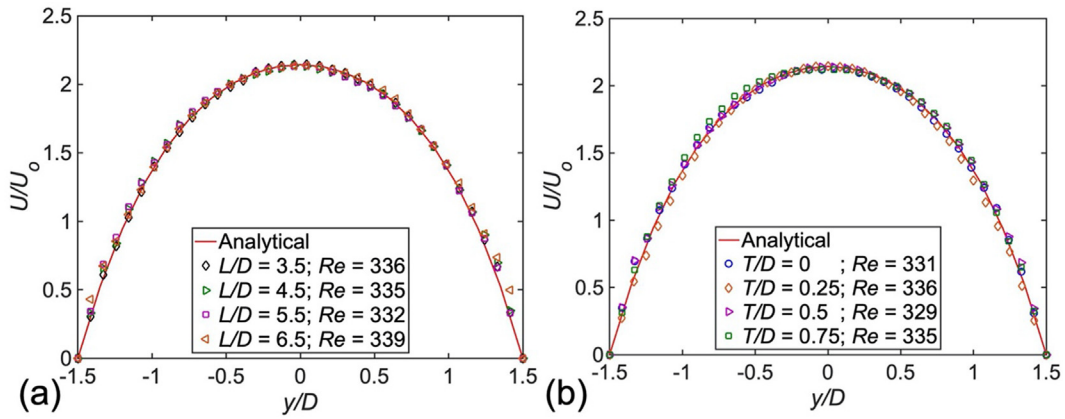

Fig. 3. Comparisons between experimental velocity profiles for microchannels with (a) T/D fixed at 0 and various L/D and (b) L/D fixed at 2.5 and various T/D as well as analytical (solid line) velocity profiles (x/D = -5, z/D = 0) for Re around 335 (exact values shown in the figure).

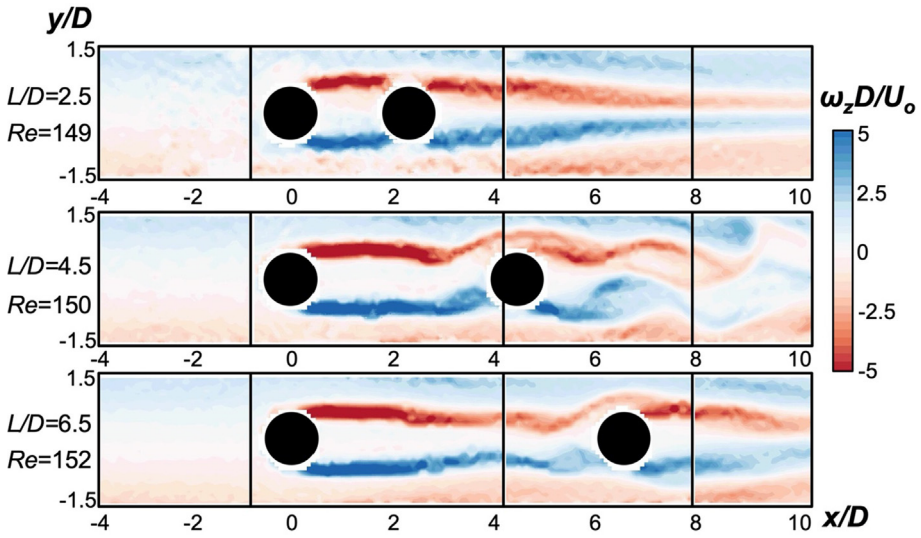

Fig. 4. Vorticity ($\omega_z D/U_o$) contours, for microchannels with tandem cylinders (T/D = 0), for L/D = 2.5 (top row), 4.5 (middle row) and 6.5 (bottom row), for Re ≈ 150 (exact values shown in the figure). The vorticity fields are composites, formed by stitching together a number of overlapping segments, as discussed in Section 2.2.

suggest that the wake dynamics are particularly sensitive to the position of the second cylinder and the channel confinement.

The flow becomes more unstable when the Reynolds number is increased to ≈300, as can be seen in the instantaneous vorticity and concentration fields in Figs. 5 and 6, respectively. Instantaneous normalized concentration fields for various L/D at different Reynolds number are shown in the Supplementary Video 2.

In the L/D = 2.5 microchannel (top row of Fig. 5 and Fig. 6), no vortex-shedding is observed behind the first cylinder, and the shear layers remain roughly parallel until they reattach to the second cylinder, with the concentration fields showing that two attached vortices inhabit the inter-cylinder gap. The sharp interface along the channel centreline in the concentration fields is maintained until x/D ≈ 8, whereupon there are some fluctuations in the layers prior to the formation of weak vortices further downstream. There is significantly greater mixing when the spacing is increased (L/D = 4.5 and 6.5); here Fig. 5 and Fig. 6 show that there is vortex-shedding from the first pin, which results in greatly increased mixing between the fluid layers. The impingement of the shed vortices on the second pin results in chaotic vortical flow in its wake and very effective mixing between the fluid layers, with the interface region (where $c/c_0 \sim 0.5$) extending across the entire width of the channel.

At intermediate values of longitudinal displacement, below the onset of vortex-shedding (L/D = 3.5), the flow is bistable, with the shear layers from the first cylinder intermittently switching between reattaching to the second cylinder (as found for L/D = 2.5) and rolling up to form vortices (as occurs for L/D ≥ 4.5). The two modes can be seen in Fig. 7 which shows examples of the shear layers reattaching (a-c) and rolling up (d-f), focussing on the inter-cylinder region where the bistable behaviour occurs. The sampling frequency in these PIV measurements is approximately an order of magnitude lower than the shedding frequency (assuming St ∼ 0.3), which means that the transitions between modes cannot be distinguished. However, it was observed that when vortex-shedding occurred, it was evident in a number of successive PIV measurements, suggesting that the mode can remain for tens of cycles. The variability in the wake dynamics means that it was not possible to stitch together the various instantaneous PIV measurements over different regions, as performed in other cases in which the flow was either steady or periodic. However, the vorticity fields in Fig. 7 clearly demonstrate that both modes can occur for microchannels with L/D ≈ 3.5, highlighting the complexity of the wake dynamics.

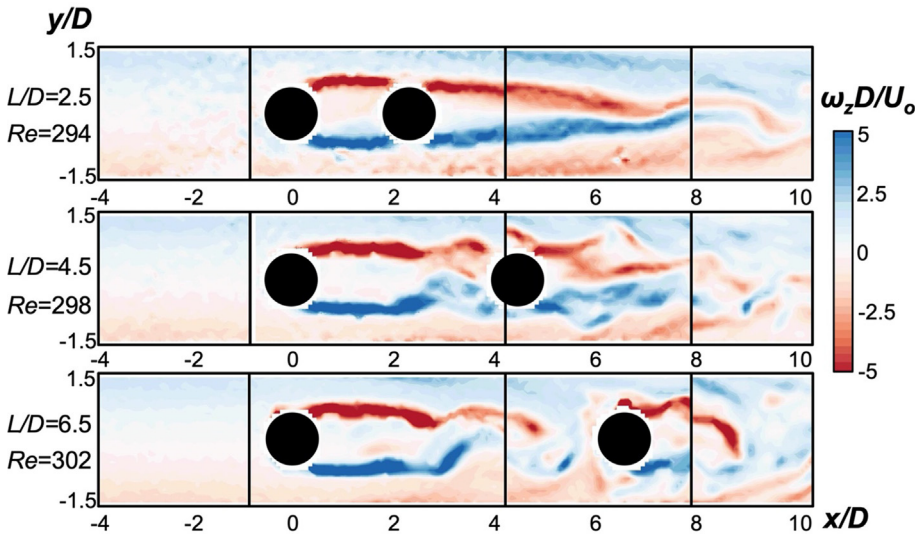

Fig. 5. Vorticity ($\omega_z D/U_o$) contours for microchannels with tandem cylinders (T/D = 0), for L/D = 2.5 (top row), 4.5 (middle row) and 6.5 (bottom row), for Re ≈ 300 (exact values shown in the figure). The vorticity fields are composites, formed by stitching together a number of overlapping segments, as discussed in Section 2.2.

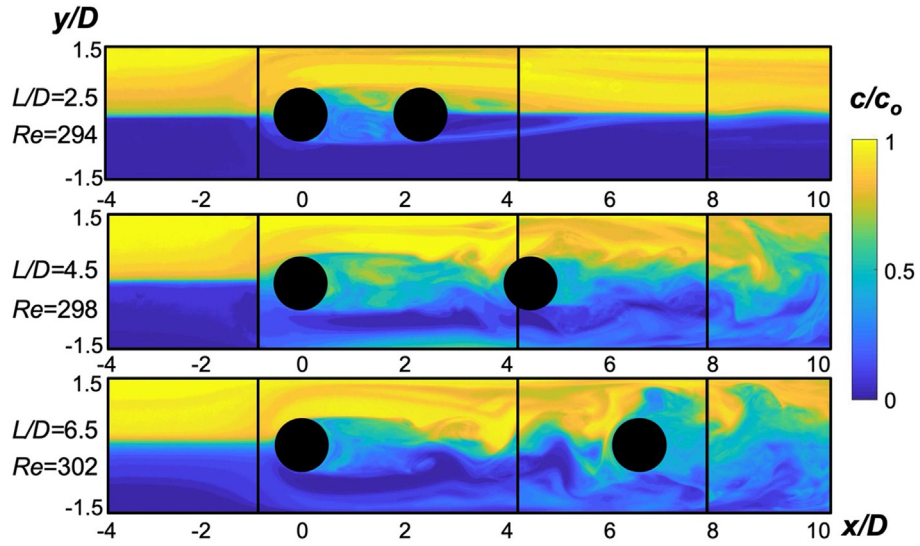

Fig. 6. Instantaneous normalized concentration fields for various L/D in the flow region −4 < x/D < 10, with the two mixing fluids interface set on the channel centreline, for Re ≈ 300. The corresponding vorticity fields are shown in Fig. 5. The fields are composites, formed by stitching together a number of overlapping segments, as discussed in Section 2.3.

3.3. Wake and interface dynamics for staggered cylinders

Selected instantaneous vorticity fields in the flow region ranging from x/D = -2 to 11 are shown in Fig. 8 for Re ≈ 150.

No vortex-shedding can be observed behind the two staggered cylinders for any choice of lateral spacing at this Re value, but significant differences can be found in the vorticity fields for varying T/D. At T/D = 0.25 (top row of Fig. 8), one of the shear layers separating from the first pin reattaches on the same side of the second one; the additional vorticity from this upstream separated shear layer causes the downstream one to appear much stronger compared to the one separating from the lower side. Increasing the spacing to T/D = 0.5 (middle row of Fig. 8) causes the upper shear layer from the first cylinder to be deflected through the gap between the two cylinders. Meanwhile, the increased transverse flow between the gaps that is responsible for the deflection of the negative shear layer also increases velocity gradients in this region and strengthens the positive shear layer attached to the second cylinder. This deflection of the shear layers from the first cylinder is also observed for T/D = 0.75; however, in this case they remain steady and by x/D ≈ 5 have largely dissipated. Interestingly, in this channel, the second cylinder is very close to the channel wall and there is no visible shear layer on the side of cylinder next to the wall, implying that the gap between the pin and the wall is so small that there is negligible flow through it. Instead, there appears to be significantly greater flow below the cylinder (y/D < 0.25), and a very long positive shear layer extends from the lower side of the cylinder into the wake.

The onset of vortex-shedding significantly alters the shear layers, wake structure and interfacial area between the two co-flowing streams for all three configurations at Re ≈ 300 (Fig. 9 and Fig. 10). For both T/D ≈ 0.25 and 0.5, the negative shear layer from the upper side of the first cylinder impinges on the second cylinder and is deflected downward, which results in the entrain-

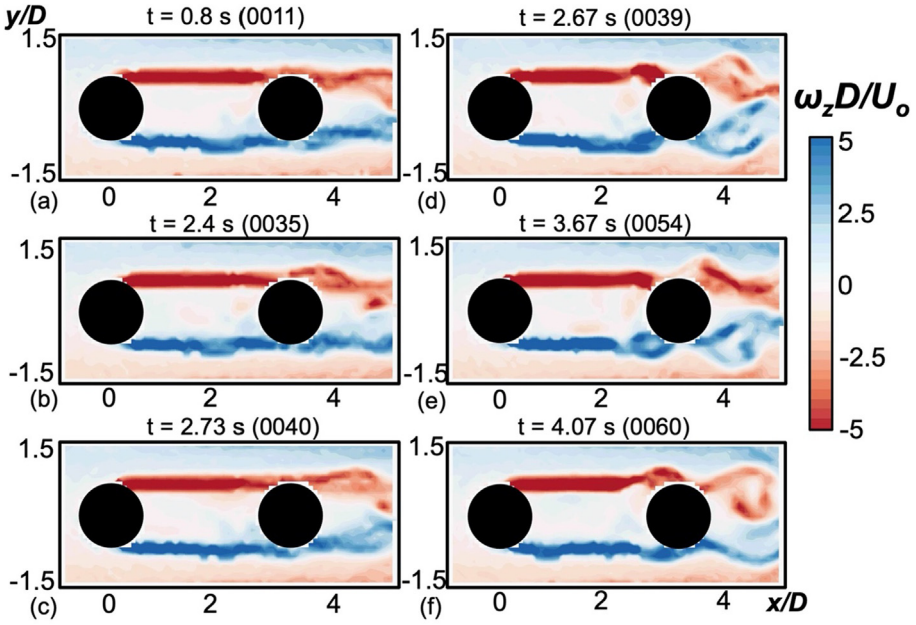

Fig. 7. Sample instantaneous vorticity fields for microchannels with tandem cylinders (L/D = 3.5), for Re = 299. The left columns (a-c) show instances in which the shear layers from the first cylinder reattached to the second cylinder, and the right column (d-f) show instances in which the shear layers roll up to form vortices before reaching the second cylinder.

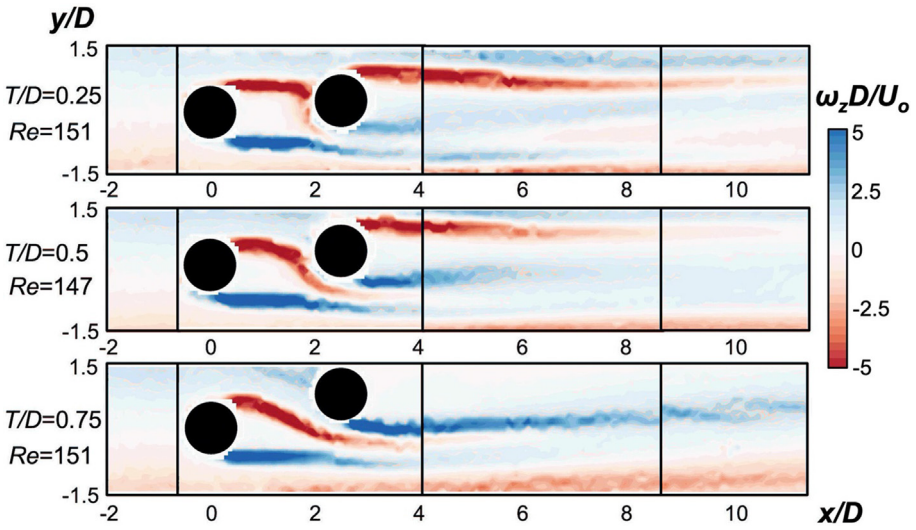

Fig. 8. Vorticity contours $\omega_z D/U_o$ for microchannels with cylinders in staggered (L/D = 2.5) and T/D ranging from 0.25 to 0.75. The Reynolds number ≈ 150 (exact values shown in labels on the left). The fields are composites, formed by stitching together a number of overlapping segments, as discussed in Section 2.2.

ment of fluid from the upper layer (yellow fluid in Fig. 10) to the lower side of the channel. The flow is chaotic in the wake of the second cylinder, resulting in strong dispersion in the concentration fields; however, in the case of T/D = 0.5, the deflection of the flow in the inter-cylinder region means that the wake is entirely comprised of fluid from the upper layer (middle row of Fig. 10). Instantaneous normalized concentration fields for various T/D at different Reynolds number are shown in the Supplementary Video 3.

The flow is again markedly different when the lateral spacing is increased to T/D = 0.75 (bottom row, Figs. 9, 10). As was the case at the lower Re (Fig. 8), the shear layers from the first pin remain stable and dissipate after a relatively short distance, and a single positive shear layer extends from the second pin far into the wake. However, in this case it begins to roll up at x/D ≈ 8. The absence of a shear layer from the opposite side of the cylinder and the apparent stability of the negative shear layer at the low wall indicate that this roll up is caused by the Kelvin-Helmhotz instability, rather than the normal vortex-shedding process in a cylinder wake.

3.4. Onset of instability in cylinder wakes

The flow patterns presented in the previous sections demonstrate the dramatic effect cylinder arrangement, confinement and Reynolds number can have on the wake dynamics. In order to characterise the unsteady behaviour established in each arrangement, the average root-mean-square of the fluctuating transverse velocity, $\langle V_{rms} \rangle / U_o$, was calculated in various regions in the wake from the ensemble-averaged PIV measurements, as shown in Supple-

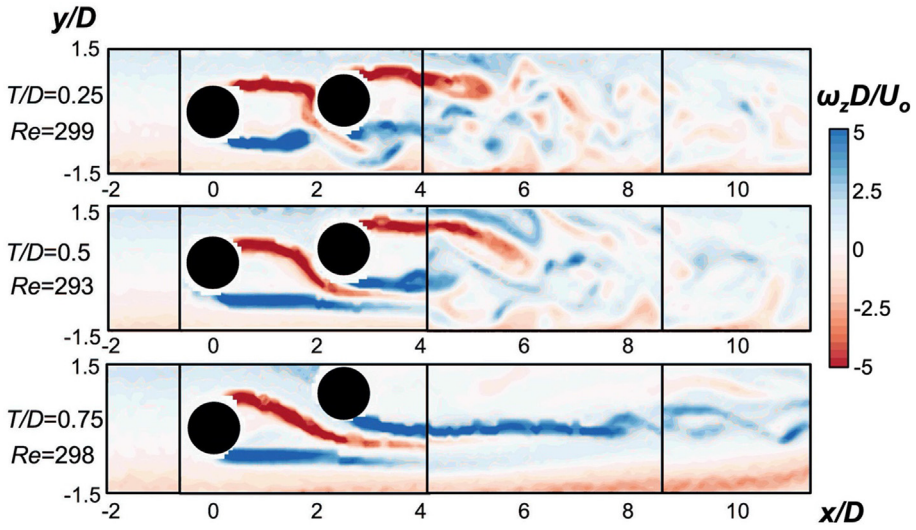

Fig. 9. Vorticity ontours $\omega_z D/U_o$ for microchannels with cylinders in staggered (L/D = 2.5) and T/D ranging from 0.25 to 0.75. The Reynolds number ≈ 300 (exact values shown in labels on the left). The fields are composites, formed by stitching together a number of overlapping segments, as discussed in Section 2.2.

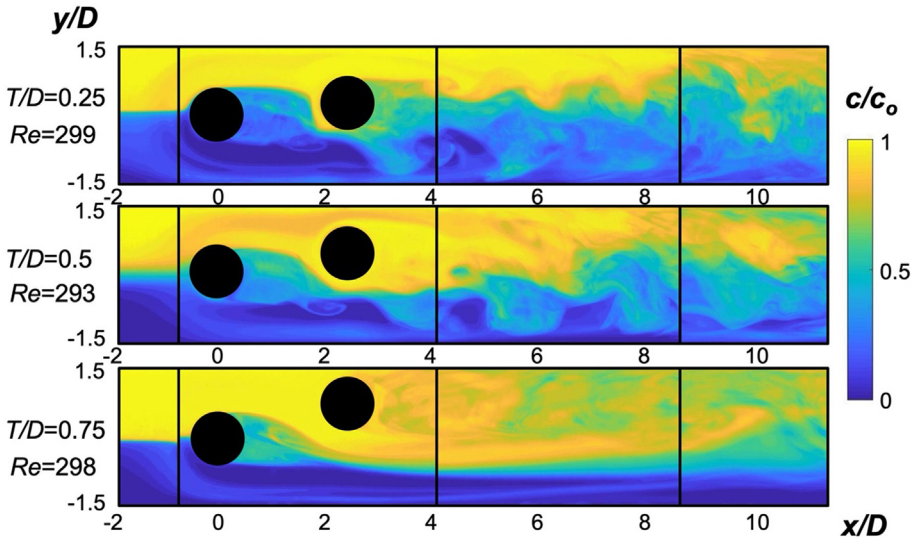

Fig. 10. Instantaneous normalized concentration fields for staggered cylinder pairs at various T/D in the flow region −2 < x/D < 11, with the position of inlet fluids interface set at the channel centreline. The Reynolds number ≈ 300 (exact values shown in labels on the left); fields correspond to vorticity maps of Fig. 9. The fields are composites, formed by stitching together a number of overlapping segments, as discussed in Section 2.3.

mentary Material S3. The regions spanned the entire channel width, but were taken at different streamwise locations, depending on the cylinder configuration. For the first cylinder, the averages were computed over the region 1D immediately upstream of the second cylinder, and for the second cylinder, 3-4D downstream of the centre of the second cylinder (e.g. for L/D = 4.5, the measurement regions were x/D = 3 – 4, and 7.5 – 8.5).

The variations in the $< V_{rms} > /U_o$ signals is shown in Fig. 11 for both the upstream and downstream cylinders (left and right columns, respectively) in tandem and staggered arrangements (top and bottom row, respectively). The differences in the locations at which $< V_{rms} > /U_o$ was measured and the different forms of instability being characterised means that care should be taken in attempting to make qualitative comparisons between the various trends in Fig. 11; however, they can be used to identify the critical Reynolds number for the onset of instability, and can provide some qualitative insight into how the various instabilities develop with Re.

For the closely spaced tandem cylinders (L/D = 2.5), the flow in the inter-cylinder region remains stable, and consequently $< V_{rms} > / U_o$ in this region is constant and of small magnitude over the entire range of Reynolds number examined (Fig. 11a), while in the wake of the second cylinder it increases gradually from about Re = 200. When the spacing is increased slightly to L/D = 3.5, bistable behaviour is observed, as discussed in section 3.2, which manifests itself as a gradual increase in velocity fluctuations starting from Re ≈ 220, in an approximately linear manner. The channels with more widely spaced tandem cylinders (L/D ≥ 4.5) all exhibit some similar features, with the velocity fluctuations increasing sharply at approximately the same Re, after which they appear to increase at a more gradual rate.

The data for the staggered channels (Fig. 11b and Fig. 11d) exhibits a great degree of variability, which is reflective of the more varied wake dynamics seen in these channels (Fig. 8 and Fig. 9). A small increase in the lateral spacing (T/D = 0.25) - compared to tandem position (T/D = 0) - induces an increase in velocity fluctu-

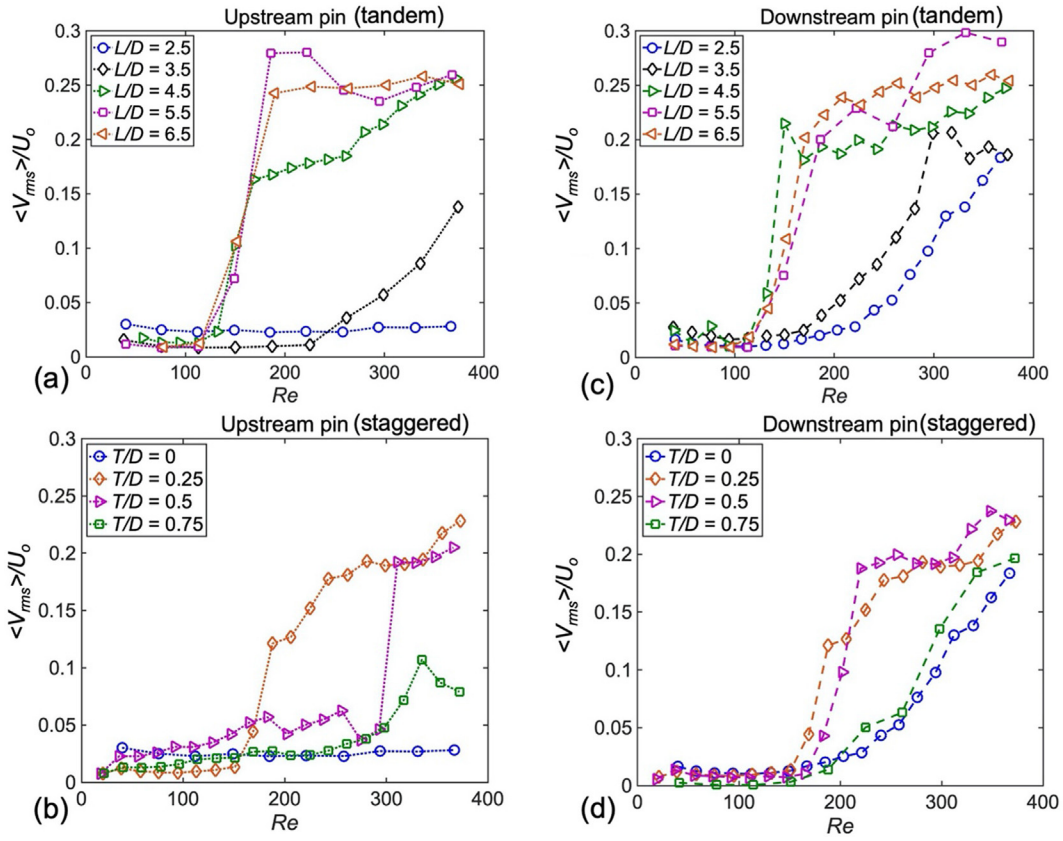

Fig. 11. Variation of the mean $< V_{rms} > /U_o$ calculated in the wake of the upstream (a) and downstream (b) tandem cylinders, and is the wake of the upstream (c) and downstream (d) staggered cylinders, for which L/D = 2.5. The regions over which the averages were calculated are discussed in the text.

ations at a relatively low Re of ≈150, which appears to be associated with the interaction of the negative shear layer from the first cylinder with the second one (Fig. 8, top row), as no vortex-shedding was seen in the μPIV measurements. Further increasing T/D to 0.5 delays this rise in velocity fluctuations, with $< V_{rms} > / U_0$ now sharply increasing at Re > ∼300. For the channel with the largest lateral spacing (T/D = 0.75), the magnitude of fluctuations in the inter-cylinder region only increases slightly at Re > 300, although the trend here is unclear. Finally, in the wake of the second cylinder, the magnitude of fluctuations tends to increase gradually (Fig. 11d), in contrast to the tandem cylinder channels, where $< V_{rms} > / U_0$ increased sharply. However, it should be noted that for T/D = 0.75 these fluctuations are associated with the Kelvin-Helmhotz instability rather than vortex-shedding.

The trends presented in Fig. 11 indicate that the various instabilities (shear layer oscillations, vortex-shedding and bimodal states) develop in a different manner; for most channels, the magnitude of $< V_{rms} > / U_0$ increases gradually with Re before appearing to start levelling off, which is consistent with a super-critical transition. For tandem cylinders with L/D ≥ 4.5, the flow becomes unstable suddenly at a given Reynolds number, after which the magnitude of the (non-dimensional) velocity fluctuations becomes much less sensitive to Re. Despite the steepness of the increase, it can be seen from Fig. 11a and Fig. 11c that there are intermediary points where $< V_{rms} > / U_0 \approx 0.05 - 0.12$, indicating that this is not in fact a discontinuity, as would be characteristic of a subcritical transition.

Sharp increases in $< V_{rms} > / U_0$ with Reynolds numbers are also observed in the inter-cylinder region (Fig. 11b) in the staggered cylinder channels for T/D = 0.25 and 0.5, although in this case it is not clear that no discontinuity exists, suggesting that the development of the shear-layer instability in this region may be due to a sub-critical transition.

The wide range of instabilities shown in the flow fields, the different growth rates of the magnitude of the instabilities with Re and potentially the existence of both super- and sub-critical transitions indicate the complexity of the flow of cylinder pairs in confined channels relative to the unconfined flows (Hosseini et al., 2021) or single cylinder (Griffith et al., 2011) and the sensitivity to channel geometry.

The trends in Fig. 11 can be used to estimate the critical Reynolds numbers for the onset of instability in the inter-cylinder region behind the first cylinder, Re_{c1}, and in the wake of the second cylinder, Re_{c2}. As mentioned above, in some cases the magnitude of fluctuations increases very gradually, depending on which instability is taking place and where in the channel, making it challenging to determine a critical Re that is applicable to all measurements. As a consequence, we take the onset of instability to be the point at which $< V_{rms} > / U_0 \geq 0.05$, which allows for comparison between cases.

The variation in Re_{c1} and Re_{c2} are presented in Fig. 12. In the most closely spaced tandem microchannel (L/D = 2.5), no significant fluctuations are observed in the inter-cylinder region and consequently no critical Reynolds number could be determined for the onset of vortex-shedding from the upstream pin. However, the presence of the upstream cylinder significantly delays the onset of vortex-shedding in the wake of the downstream cylinder compared to the single cylinder case. Re_{c2} is reduced somewhat when the spacing is increased to L/D = 3.5, and onset of the bimodal instability in the shear layers from the first cylinder occurs at Re ≈ 280 (although Fig. 11 indicates that these bimodal variations

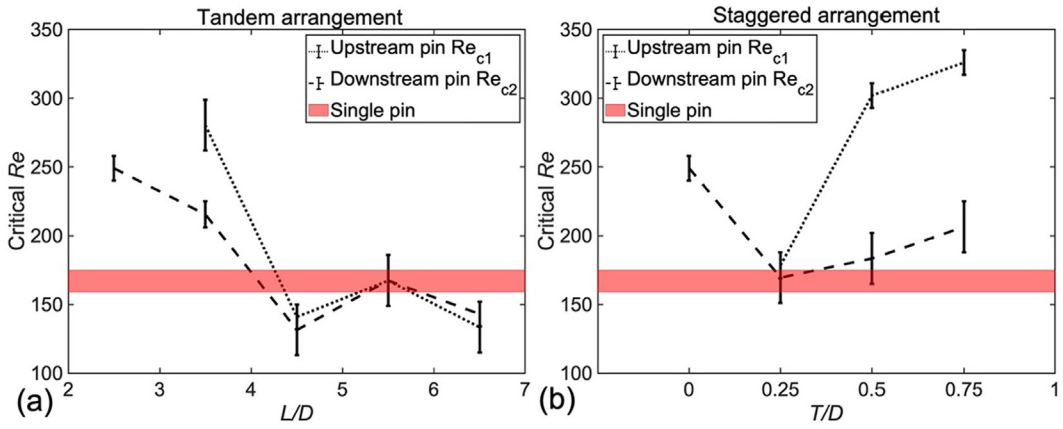

Fig. 12. Variation in the critical Reynolds number for the onset of instability in the wake of the first and second cylinders, as a function of cylinder spacing in microchannels with tandem cylinders (a) and as a function of lateral spacing in microchannels with staggered arrangements and L/D = 2.5 (b). The red band indicates the equivalent value for a single cylinder under the same confinement (Zhang et al., 2019). The error bars for two-cylinder data and the thickness of the red band for the single cylinder case indicate the uncertainty in the estimate of the critical Re, based on the resolution of Re achieved with our setup. (For interpretation of the references to colour in this figure legend, the reader is referred to the web version of this article.)

may have begun earlier, at approximately Re = 200, but were of a small magnitude).

At higher L/D (>4.5), the value of critical Re is close to that of a single pin. However, despite the similarity in the critical Reynolds numbers, the tandem cylinders display dynamics that are distinct from those seen in channels with a single pin. The vorticity and concentration fields at Re ≈ 300 (Fig. 9 and Fig. 10) show that for L/D ≥ 4.5 vortices shed from the first cylinder induce chaotic behaviour in the wake of the second; Fig. 12 indicates that this instability in both wakes is induced at approximately the same Reynolds number. However, for L/D = 4.5 and 6.5, Re_{c1} and Re_{c2} are not equal. For L/D = 4.5, the downstream wake becomes stable first, while for L/D = 6.5 it is the upstream cylinder that becomes unstable first. In both cases the critical Reynolds numbers are below that for the single cylinder, implying that the instability from one cylinder is triggering instability on the other.

For L/D = 2.5, offsetting the downstream cylinder by T/D = 0.25 leads to a dramatic reduction in the critical Reynolds numbers, which now both occur within the range predicted for a single cylinder. Returning to the flow vorticity fields at Re ≈ 300 (Fig. 9), vortices can only clearly be seen in the wake of the second cylinder, and the velocity fluctuations in the inter-cylinder region may arise in part from oscillations in the shear layers caused by the roll up of vortices nearby (in the near wake of the downstream cylinder). However, in the concentration fields in Fig. 10 (top row), a faint vortex can be seen at x/D ≈ 1.5, indicating that these fluctuations are also due to vortex-shedding. A similar vortex is present at x/D ≈ 2 in the middle row of Fig. 10 (T/D = 0.5), although in this channel this shedding only occurs for Re > 300, while in the wake of the second cylinder, vortex-shedding occurs at a similar Reynolds number to that of T/D = 0.25 and the tandem case. Finally, in the channel with the most offset cylinder, T/D = 0.75, Re_{c2} is estimated to be ≈210. However, the gradual increase of $< V_{rms} > /U_0$ in Fig. 11d indicates that the Kelvin-Helmhotz instability has begun at a lower Re but only reaches the threshold value of 0.05 at Re = 210.

3.5. Vortex-Shedding frequency

In order to gain deeper insight into the vortex-shedding dynamics of the two confined cylinders in tandem, the shedding frequency was determined using the time-resolved velocity measurements. The instantaneous transverse velocity signal at selected points (at least three points) from 9000 image pairs was used to determine the shedding frequency f and the corresponding Strouhal number; the latter was given by St = fD/U_m, where U_m is the maximum velocity of the approaching flow as measured in Section 3.2, to be consistent with previous studies in the literature. The maximum standard deviation in the measured frequencies was 2.8 % of the mean. Due to the frame rate limitation of the high-speed camera (up to 36,000 Hz for the desired viewing window), reliable shedding frequency results could only be captured for Re < 260, which meant that St could not be measured for L/D = 2.5 or 3.5 in tandem arrangement. For brevity, selected Fast Fourier Transform (FFT) spectra at different Re for microchannels with L/D = 2.5 and T/D ranging from 0.25 to 0.75 are shown in the Supplementary Material S4.

The variation of the Strouhal number with Re for channels with tandem and staggered cylinders are shown in Fig. 13, as well as the St found for a microchannel containing a single pin and the same confinement ratios (Zhang et al., 2019). For the tandem cylinders with L/D ≥ 4.5, the Strouhal number is reduced relative to the single cylinder case. In each case the shedding frequency from the first and second cylinder are approximately equal, indicating that the shedding processes behind each cylinder are coupled.

The reduction in the shedding frequency when a second cylinder is added to the channel may be explained in terms of Roshko's hypothesis of a universal Strouhal number for all bluff bodies, which depends not on the diameter of the body but on the width of the near wake, D_w (Roshko, 1955, 1954). Similar definitions have been suggested by other authors (Bearman, 1967; Griffin, 1980). In the case of a single cylinder, the shear layers are not parallel to the channel walls but are instead deflected slightly towards the centre of the channel (Zhang et al., 2019). However, the second cylinder prevents this shifting of the shear layers (see Fig. 5, where the shear layers remain parallel to the channel walls). This leads to a larger D_w compared to the single cylinder, and therefore (according to Roshko's proposed scaling) a smaller vortex-shedding frequency.

For the staggered cylinder channels, no dominant frequency peak could be detected for T/D = 0.75, in which the unsteadiness was caused by shear-layer roll up in the far wake rather than vortex-shedding. For the slightly offset cylinder, T/D = 0.25, the Strouhal number is now larger than for the single cylinder channel, and the shedding from both cylinders are synchronised. When T/D = 0.5, the Strouhal number for the downstream cylinder is

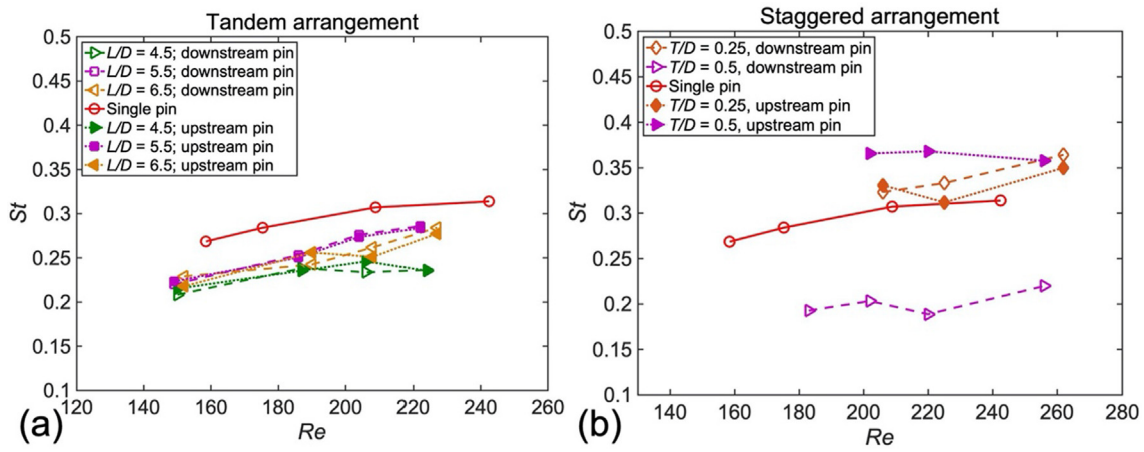

Fig. 13. Variation of St with Re for various values of L/D in channels with tandem cylinders (a) and T/D in channels with offset cylinders and L/D = 2.5 (b). The short-dashed and long-dashed lines represent the upstream and downstream cylinders, respectively, while the red circles denote the values found for a single cylinder under the same confinement. (For interpretation of the references to colour in this figure legend, the reader is referred to the web version of this article.)

increased further, while St for the upstream cylinder is reduced to approximately half that of the downstream cylinder. Referring to the flow visualisation in this channel at similar Re (Fig. 10, middle row), we can see that a vortex is shed from the bottom cylinder but there is no such shedding from the upper side. This will result in a doubling of the period of velocity fluctuations and a halving of the Strouhal number, as seen here.

The increases in St here are also consistent with Roshko's hypothesis, as the vorticity fields in this Re range (Fig. 9) indicate that the shear layers are forced to converge as they are deflected downward by the second cylinder. This is particularly clear in the T/D = 0.5 channel. However, care should be taken in this case, as these flows are highly asymmetric which was not considered by Roshko. Furthermore, the deflection of the shear layers will alter the base pressure, which was a key factor in his analysis.

3.6. Comparison to unconfined flows

It is interesting to compare the observations presented in the preceding sections to data from the literature for pairs of cylinders in unconfined flows. Several previous researchers have examined the various shedding modes seen behind a wide variety of cylinder configurations (typically at higher Reynolds number compared to what was achieved in our experiments or most microfluidic applications), which has led to a number of regime maps, as well as some conflicting systems of nomenclature.

The reviews by Sumner (2010) and Zdravkovich (1987) summarise the various regimes for tandem cylinders: when the cylinders are closely spaced (L/D < 2), they act as a single bluff body; slightly further apart they inhabit the 'reattachment regime' (2 < L/D < 5) in which the shear layers from the upstream cylinder reattach to the downstream cylinder; and at higher spacing (L/D > 5) vortex-shedding occurs at the same frequency from both cylinders (the 'co-shedding regime'). At the transition from the reattachment and co-shedding regimes, the flow is bistable, with the shear layers from the first cylinder intermittently reattaching to the second, which was found to occur in unconfined flow at L/D ≈ 3.5 for Re > 1.5×10^4 by Igarashi (1981) and at L/D = 4 for Re = 300 by Xu and Zhou (2004). The vorticity fields in Fig. 5 are consistent with these findings; bistable flow occurs at L/D = 3.5, with the reattachment regime occurring at smaller L/D and co-shedding occurring when the spacing is larger.

Further comparison between the confined and unconfined cases can be drawn by examining the dependence of the frequency of vortex-shedding on the cylinder spacing found from our experiments and those in unconfined flow (Li et al., 1991; Sharman et al., 2005; Xu and Zhou, 2004), as shown in Fig. 14. The values are normalised by the Strouhal number of a single cylinder, St_0, in order to account for the fact that the shedding frequency depends on the lateral and axial confinement. While no data was available for the cases with L/D < 4.5 (due to framerate limitations of our camera), Fig. 14 indicates that again the results for our microchannels are consistent with those of unconfined flow, even when there is an order of magnitude difference in Reynolds number (Xu and Zhou, 2004).

The agreement between the flow regimes and the effect of L/D on the Strouhal number recorded here and the results from various studies in unconfined flow is surprising, and suggests that the wake dynamics of tandem cylinders is remarkably insensitive to the degree of confinement, even when W/D and H/D are reduced to 3.

The effect of confinement on the flow is more visible when the cylinder is offset from the channel centreline. Xu and Zhou (2004) performed flow visualisation in unconfined flow at Re = 300, allowing straightforward comparison to our data. Based on the regime map they presented, for L/D = 2.5 and T/D = 0 and 0.5, the shear

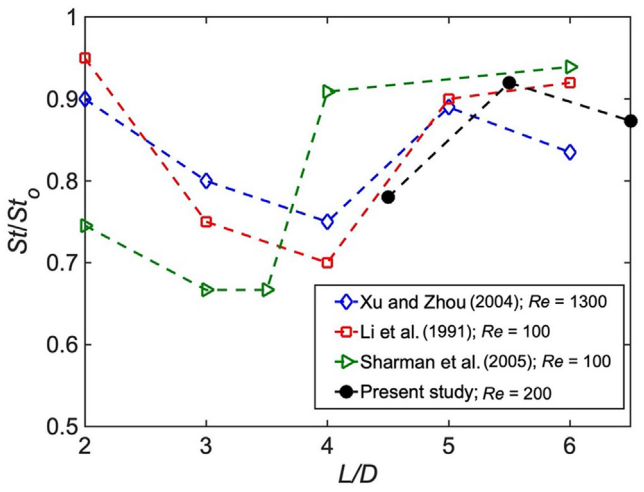

Fig. 14. The effect of longitudinal pitch ratio L/D on Strouhal number for two tandem cylinders in cross-flow at Re of 1300 (Xu and Zhou, 2004), 100 (Li et al., 1991; Sharman et al., 2005) and 200 (present study).

layer reattachment (SLR) mode (Sumner, 2010) would be expected, in which the wake is characterised by a von Karman vortex street by x/D > 6.5 (equivalent to the reattachment regime). When the lateral spacing is increased to T/D = 0.5 and 0.75, a single vortex street is again expected but with a strong asymmetry in strength of vortices and different shedding frequencies from both cylinders (the synchronized vortex-shedding (SVS) mode (Sumner, 2010)).

The vorticity field in Fig. 9 for T/D = 0.25 shows some similarities with the SLR mode in the near wake (i.e. the shear-layer from the first cylinder reattaches to the second), but instead of forming a far wake similar to the von Karman vortex street, no large, coherent vortices can be identified for x/D > 8. Similarly, for T/D = 0.5, the new wake of the downstream cylinder matches the regime predicted by Xu and Zhou (2004), (i.e. the formation of a single vortex street), no large-scale vortices are observed in the far wake. In both cases the wake in the region 5 < x/D < 8 is characterised by irregular filaments and spots of vorticity, which have largely dissipated by x/D ≈ 10. The absence of a clear vortex street compared to the unconfined flows at the same Re implies that the channel confinement is responsible for the dissipation of vorticity, most likely through the addition of alternate-signed vorticity from the boundary layers along the channel walls.

A similar breakdown in the vortex street is observed for T/D = 0.5 (Fig. 6 middle row), and the vorticity field is too disorganised to identify an asymmetry in the vortices, as occurs in the SVS mode in unconfined flow (Xu and Zhou, 2004). Likewise, the confinement at T/D = 0.75 completely disrupts the normal vortex-shedding process and the vorticity field bears no similarity to the SVS mode. Instead, the flow is rather similar to the pattern around a circular cylinder close to a wall (Wang and Tan, 2008), indicating that the presence of the wall plays a more important role in determining the wake dynamics than the presence of the upstream cylinder.

While the confinement has a relatively minor effect on the flow for tandem cylinders, it is clear that lateral confinement is capable of completely disrupting the regime map. The greater sensitivity of confined flow to lateral displacement of cylinders is somewhat intuitive, as it can lead to very small gaps and an even greater local confinement. Furthermore, the induced asymmetry in the flow is greater when the confinement is large, as disparity in the gap flow on either side is pronounced by the boundary layers. This is most clear in the T/D = 0.75 channel, where the gap at the upper side of the channel is reduced to only 0.25D, and the velocity deficit in the boundary layer close to the wall means that very little fluid moves through this gap, creating a stagnation region (Fig. 6 and Fig. 9, bottom row). Instead, it is rather similar to the pattern around a circular cylinder close to an end wall (Wang and Tan, 2008), indicating that the presence of the wall plays a more important role in determining the wake dynamics than the presence of the upstream cylinder.

3.7. Mixing performance

For each location, the mixing index was computed from the average of M on 100 concentration strips acquired at each Re, as explained in Section 2.3. The variation in M in the streamwise direction is shown in Fig. 15a, corresponding to the data sets in Fig. 6. Upstream of the pins, in the region x/D < -1, mixing is relatively weak in all cases (M<10 %). For the L/D = 2.5 case (reattachment regime), there is a local increase in mixing in the wake of the first cylinder due to the attached vortices, but there is only a very small increase (approximately 5 %) in M as the fluid exits the μLIF measurement domain (at x/D = 15). Considering that M increases from 0 to 10 % in the entry region before entering the measurement region at x/D = -5, (i.e. a distance of ≈100D), and the length of the measurement region is 20D, as first order approximation, we could expect M to increase by around 2 % over the measurement region in the absence of pins. Therefore, in the reattachment regime, the addition of pins leads to only a marginal increase in mixing performance.

The pins are slightly more effective for L/D = 3.5, with M reaching 38 % by x/D = 15, which is likely a result of the bistable flow that occurs therein. In contrast, in the co-shedding regime (L/D ranging from 4.5 to 6.5) we see a dramatic increase in the mixing index, reaching approximately 60 % in all cases.

The dependence of mixing performance with Reynolds number is demonstrated in Fig. 15b, where the change in mixing index, ΔM (from the streamwise location x/D = -3 to 14) is plotted as a function of Re for the various L/D values investigated. The range of x/D is chosen to facilitate comparison to the case of a single pin (red circles (Zhang et al., 2020)). For L/D = 2.5 (blue symbols), the mixing enhancement remains always low (<10 %), even for Re greater than the critical value for the onset of vortex-shedding (around 260). As was shown in Fig. 11, the magnitude of the transverse fluctuating velocity (V_{rms}/U_o) remains low in the wake of both pins (<0.03 and 0.15 respectively), even for a Re of 300 in this configuration, in comparison to the longer pitch ones. This indicates that even with the onset of vortex-shedding, the flow instability has no effect on mixing as it does not significantly disrupt the interface between the two fluids further downstream from the wake. Similar trends are observed for the other case in the reattachment regime (L/D = 3.5), until Re ≈ 300, at which point the onset of vortex-shedding leads to a significant increase in mixing (ΔM > 30 %). The difference in mixing performance between the two configurations can be explained by the corresponding increase in the velocity fluctuations in the wake of the upstream cylinder when L/D is increased to 3.5 (Fig. 11a).

All three cases in the co-shedding regime (L/D ≥ 4.5) show remarkably similar results that are similar to the single pin case; ΔM remains low until the onset of vortex-shedding at Re ≈ 300, where it increases sharply, and then continues to increase gradually with Re, reaching ΔM = 55 – 60 % by x/D = 15. Again, these trends in the magnitude of mixing enhancement can be closely linked with the variations in $< V_{rms} > /U_o$ seen in Fig. 11a (a sudden jump at the critical Re, followed by a gradual increase, with all cases in the co shedding regime showing similar results).

Based on the above results, it can be concluded that in the microchannels with two cylinders in tandem and located at the channel centreline (i.e. symmetric confined cylinders), no significant mixing enhancement is seen below the critical Reynolds number, or in the reattachment regime, highlighting the importance of vortex-shedding in dispersing the fluid phases.

It is also notable that the addition of a second cylinder that is in-line with the upstream cylinder, only leads to a slight increase in mixing performance in the co-shedding regime (as well as actively suppressing mixing in the reattachment regime). However, the introduction of the second cylinder will be associated with an increased pressure drop, which may lead to a reduced flow rate and throughput, an important consideration when designing micromixers.

The corresponding variation in the mixing index M for the staggered cylinder microchannels is shown in Fig. 15c for Re ≈ 300, which corresponds to the concentration fields presented in Fig. 10. Previous work examining microchannels with a single pin (Zhang et al., 2019) and the LIF measurements discussed previously (Fig. 10) have shown that mixing in asymmetric channels occurs primarily via two mechanisms; the steady convective mixing caused by the transverse flows induced by the offset pin and the unsteady convective mixing due to the presence of vortex-shedding (Zhang et al., 2020).

Fig. 15c shows that, as before, M is relatively low (<10 %) in the region upstream the first cylinder (x/D from −5 to −1) in all

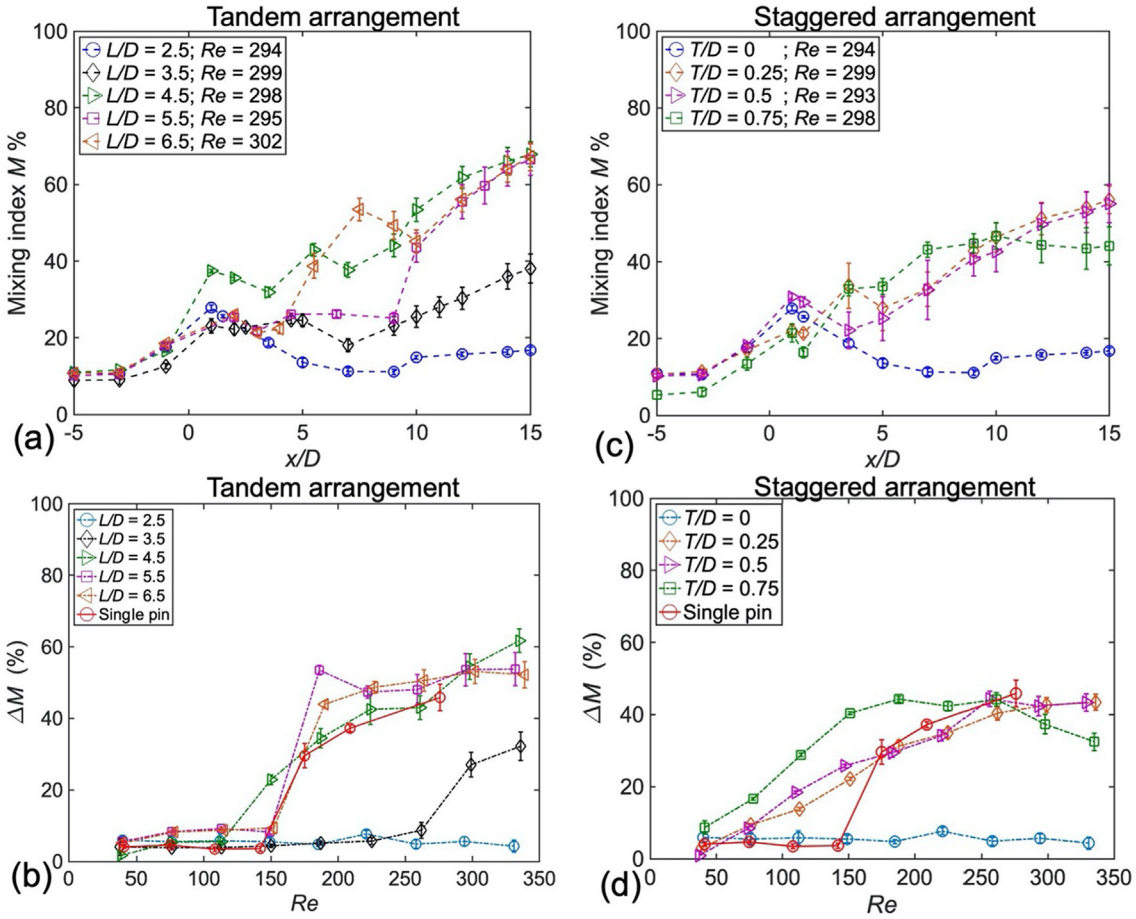

Fig. 15. The variation of the mixing index along the channel (x/D = -5 to 15) for channels with tandem cylinders (a) and staggered cylinders (c) at Re ≈ 300, and the percentage increase in M over the measurement region as a function of Re for tandem (b) and staggered (d) cylinders. Note that some of the symbols are larger than the error bars, which are computed as the standard deviation over the 100 fields.

microchannels. For T/D = 0, there is a small increase near the cylinder, but the mixing index returns to its upstream value by about x/D = 5. In contrast, for T/D = 0.25 and 0.5, vortex-shedding occurs at this Re, and a large and sustained increase is seen. The trends for both channels are closely aligned, reaching around 55 % by the end of the measurement domain (x/D = 15). In the T/D = 0.75 microchannel, the significant transverse flow in the inter-cylinder region and the recirculation in the stagnant region lead to an increase in the mixing index, but M reaches a slightly smaller maximum value of about 45 %, reflecting the weaker mixing in the absence of the shedding of alternate vortices. The unsteady convective mixing which coincides with vortex-shedding results in a steady growth of M with x/D (see Fig. 15c), whereas the steady convective mixing (due to the transverse flow or other three-dimensional flow structures) is limited to the near pin region and does not propagate further downstream. The latter effect arises because in steady convection, intense mixing is mostly confined to the recirculation region in the near wake, which does not exchange fluid with the rest of the flow. In all cases the mixing performance still seems much better than the tandem case.

Fig. 15d shows the variation of the level of mixing enhancement ΔM (the increase of M from x/D = -3 to 14) with Re. The result from a single confined pin is shown as a reference (Zhang et al., 2020). In the microchannel with L/D = 2.5 and T/D = 0, in which vortex-shedding does not occur, the mixing performance is always low (<10 %). With small offsets of the second cylinder (T/D = 0.25 and 0.5), the ΔM trends are closely aligned, increasing with Re and appearing to plateau at ΔM ≈ 42 % at around Re = 300. For the T/D = 0.75 microchannel, this ΔM reaches this level at around Re = 180, prior to the onset of vortex-shedding, and decreases slightly for Re > 260, indicating that the roll-up of the single shear layer in the far wake does not significantly disrupt the interface between the two fluids or enhance mixing.

A notable feature from the results presented in Fig. 15 is that all cases, including the single-pin microchannel, tend to have a peak mixing enhancement of ΔM ≈ 40–45 %, regardless of whether vortex-shedding is taking place. In fact, the increase in ΔM in the highly offset channel (T/D = 0.75) occurs at the lowest Reynolds number, highlighting the importance of the lateral alignment of pins in microchannel designs, and indicating that it is not always necessary to increase Re to achieve effective mixing (which may require high pressure drops in small microchannels or when using more viscous fluids).

The results indicate the importance of the pin layout and flow regime in optimising micromixers with obstacles. This was also illustrated in a recent study on micromixer design by Antognoli et al. (2021); using 20 pillar sequences with various pillar sizes and offsets and various optimisation functions mixing indices from 40 to 80 % could be achieved for Re < 100. A trade-off between mixing performance and pressure drop was demonstrated through an optimal spacing between pillars. The present work covers a wider range of Re numbers and mixing induced by instabilities rather than interface stretching by the geometry alone; it can thus help

extend such optimisation tools to unsteady flow regimes and potentially lead to more efficient micromixer design.

4. Conclusion

The flow past two confined cylinders in tandem and staggered arrangements inside microchannels was examined experimentally for various Reynolds number (up to 340). μPIV was used to characterize the flow patterns, and μLIF to acquire the instantaneous concentration fields and analyse the mixing performance. High-speed μPIV was also applied to measure the vortex-shedding frequency.

With the confined pins in tandem arrangement, the critical longitudinal pitch ratio for the onset of vortex-shedding was found to be around 3.5 at Re of 300. Compared to the unconfined cases, the confinement does not influence the appearance of bistable flow at this critical value of L/D but the Re at which it appears. With L/D less than the critical value, the two cylinders were in the 'reattachment regime', where the shear layers from the first cylinder attached to the second cylinder, resulting in the suppression of vortex-shedding. With L/D over the critical value, the two pins were in 'co-shedding regime', with the vortex-shedding frequency behind the two cylinders synchronized. The Strouhal number in this co-shedding mode was however slightly lower than that of a single cylinder in same confinement. With respect to mixing, no enhancement was observed before the onset of vortex-shedding. Once the vortex-shedding initiated, the mixing increased significantly and exceeded that for the single cylinder case. The best mixing performance was found in the microchannel with L/D = 4.5 at the highest examined Re.

For two cylinders in staggered arrangement, the suppression of vortex-shedding caused by the cylinder configuration was not trivial but mainly depended on the distance between the offset cylinder and the channel walls. In the staggered configurations with a constant longitudinal pitch ratio (L/D of 2.5), shear layer reattachment flow pattern was seen with T/D = 0.25, where the shedding frequency behind the two cylinders was the same. For T/D = 0.5, the induced separation (IS) flow pattern was observed and two Strouhal numbers were detected. The shedding frequency behind the first cylinder was much higher than the second cylinder due to the shorter and narrower wake. Therefore, when the first cylindrical pin is located at the channel centreline, the arrangement of the cylinders has the strongest effect on shedding frequency when the second cylinder is slightly offset from the channel centreline (T/D = 0.25 and 0.5). For T/D = 0.75, the second cylinder was very close to the channel wall, resulting in a single long shear layer and a long recirculation area as well as vortex-shedding suppression. Hence, the confinement from the channel walls plays a more significant role in the two pin staggered configurations than the tandem one. With Re less than the critical value for the onset of instability, cylinders in staggered arrangement have better mixing performance than the single cylinder with wall proximity proving advantageous (e.g. T/D = 0.75 case), which is attributed to steady mixing induced by the alignment of the pins. However, with Re higher than 260, the mixing enhancement in the channels with T/D = 0.25 and 0.5 exceeded that of the T/D = 0.75 channel and approached that of a single cylinder case. Therefore, these results indicate that roll up of the single shear layer in this microchannel is not sufficient to disrupt the interface between the two mixing fluids. Hence, confined cylinders with staggered arrangement can provide better mixing performance at low Re (less than the critical value for onset of vortex-shedding). At high Re, the best mixing index can be found in the microchannel with two pins in tandem and in 'co-shedding' regime (L/D over critical longitudinal pitch ratio).

Additional parameters such as lateral and vertical confinement (i.e. different channel widths and depths) are expected to influence the flow and mixing performance of the pin microchannels and will be the subject of our future work.

CRediT authorship contribution statement

Shigang Zhang: Conceptualization, Methodology, Investigation, Formal analysis, Writing – original draft, Writing – review & editing. **Yuang Han:** Methodology, Investigation, Formal analysis. **Tom Lacassagne:** Methodology, Investigation, Formal analysis, Writing – review & editing. **Neil Cagney:** Methodology, Investigation, Formal analysis, Writing – review & editing. **Carolina P. Naveira-Cotta:** Methodology, Formal analysis, Writing – review & editing, Supervision. **Stavroula Balabani:** Methodology, Formal analysis, Writing – review & editing, Supervision, Project administration. **Manish K. Tiwari:** Methodology, Formal analysis, Writing – review & editing, Supervision, Project administration, Funding acquisition.

Data availability

Data will be made available on request.

Declaration of Competing Interest

The authors declare that they have no known competing financial interests or personal relationships that could have appeared to influence the work reported in this paper.

Acknowledgements

Funding from EPSRC projects (EP/M029573/1 and EP/N024915/1) and the European Research Council (ERC) under the European Union's Horizon 2020 research and innovation programme under grant agreement no. 714712 is acknowledged. C. P.N.C. acknowledges the Visiting Researcher fellowship provided by CAPES/INMETRO, Brazil facilitating her one year visit to UCL Mechanical Engineering, U.K.

Appendix A. Supplementary material

Supplementary data to this article can be found online at https://doi.org/10.1016/j.ces.2022.118349.

References

Antognoli, M., Stoecklein, D., Galletti, C., Brunazzi, E., Di Carlo, D., 2021. Optimized design of obstacle sequences for microfluidic mixing in an inertial regime. Lab Chip 21 (20), 3910–3923.

Aparecido, J.B., Cotta, R.M., 1990. Thermally developing laminar flow inside rectangular ducts. Int. J. Heat Mass Tran. 33, 341–347. https://doi.org/10.1016/0017-9310(90)90103-2.

Aubin, J., Ferrando, M., Jiricny, V., 2010. Current methods for characterising mixing and flow in microchannels. Chem. Eng. Sci. 65, 2065–2093. https://doi.org/10.1016/j.ces.2009.12.001.

Bamshad, A., Nikfarjam, A., Khaleghi, H., 2016. A new simple and fast thermally-solvent assisted method to bond PMMA–PMMA in micro-fluidics devices. J. Micromech. Microeng. 26 (6), 065017.

Bearman, P.W., 1967. On vortex street wakes. J. Fluid Mech. 28, 625–641. https://doi.org/10.1017/S0022112067002368.

Bhagat, A.A.S., Papautsky, I., 2008. Enhancing particle dispersion in a passive planar micromixer using rectangular obstacles. J. Micromech. Microeng. 18 (8), 085005.

Bhagat, A.A.S., Peterson, E.T.K., Papautsky, I., 2007. A passive planar micromixer with obstructions for mixing at low Reynolds numbers. J. Micromech. Microeng. 17, 1017–1024. https://doi.org/10.1088/0960-1317/17/5/023.

Cantwell, B., Coles, D., 1983. An experimental study of entrainment and transport in the turbulent near wake of a circular cylinder. J. Fluid Mech. 136, 321. https://doi.org/10.1017/S0022112083002189.

Chen, W., Ji, C., Alam, M.M., Williams, J., Xu, D., 2020. Numerical simulations of flow past three circular cylinders in equilateral-triangular arrangements. J. Fluid Mech. 891, A14. https://doi.org/10.1017/jfm.2020.124.
Chen, L., Wang, G., Lim, C., Seong, G.H., Choo, J., Lee, E.K., Kang, S.H., Song, J.M., 2009. Evaluation of passive mixing behaviors in a pillar obstruction poly (dimethylsiloxane) microfluidic mixer using fluorescence microscopy. Microfluid. Nanofluid. 7, 267–273. https://doi.org/10.1007/s10404-008-0386-1.
Costa Junior, J.M., Naveira-Cotta, C.P., de Moraes, D.B., Inforçatti Neto, P., Maia, I.A., da Silva, J.V.L., Alves, H., Tiwari, M.K., de Souza, C.G., 2020. Innovative metallic microfluidic device for intensified biodiesel production. Ind. Eng. Chem. Res. 59, 389–398. https://doi.org/10.1021/acs.iecr.9b04892.
Dundi, T.M., Raju, V.R.K., Chandramohan, V.P., 2019. Characterization of mixing in an optimized designed T-T mixer with cylindrical elements. Chin. J. Chem. Eng. 27, 2337–2351. https://doi.org/10.1016/j.cjche.2019.01.030.
Dusting, J., Balabani, S., 2009. Mixing in a Taylor-Couette reactor in the non-wavy flow regime. Chem. Eng. Sci. 64, 3103–3111. https://doi.org/10.1016/j.ces.2009.03.046.
Galletti, C., Mariotti, A., Siconolfi, L., Mauri, R., Brunazzi, E., 2019. Numerical investigation of flow regimes in T-shaped micromixers: benchmark between finite volume and spectral element methods. Can. J. Chem. Eng. 97, 528–541. https://doi.org/10.1002/cjce.23321.
Geyer, T.F., 2022. Experimental investigation of flow and noise control by porous coated tandem cylinder configurations. AIAA J. 60, 4091–4102. https://doi.org/10.2514/1.J061180.
Griffin, O.M., 1980. Vortex-excited cross-flow vibrations of a single cylindrical tube. J. Press. Vess. T. 102, 158–166. https://doi.org/10.1115/1.3263315.
Griffith, M.D., Leontini, J., Thompson, M.C., Hourigan, K., 2011. Vortex shedding and three-dimensional behaviour of flow past a cylinder confined in a channel. J. Fluid Struct. 27, 855–860. https://doi.org/10.1016/j.jfluidstructs.2011.02.007.
Griffith, M.D., Lo Jacono, D., Sheridan, J., Leontini, J.S., 2017. Flow-induced vibration of two cylinders in tandem and staggered arrangements. J. Fluid Mech. 833, 98–130. https://doi.org/10.1017/jfm.2017.673.
Hoffmann, M., Schlüter, M., Räbiger, N., 2006. Experimental investigation of liquid–liquid mixing in T-shaped micro-mixers using μ-LIF and μ-PIV. Chem. Eng. Sci. 61, 2968–2976. https://doi.org/10.1016/j.ces.2005.11.029.
Hosseini, N., Griffith, M.D., Leontini, J.S., 2021. Flow states and transitions in flows past arrays of tandem cylinders. J. Fluid Mech. 910, A34. https://doi.org/10.1017/jfm.2020.975.
Hsieh, S.S., Lin, J.W., Chen, J.H., 2013. Mixing efficiency of Y-type micromixers with different angles. Int. J. Heat Fluid Fl. 44, 130–139. https://doi.org/10.1016/j.ijheatfluidflow.2013.05.011.
Igarashi, T., 1981. Characteristics of the flow around two circular cylinders arranged in tandem: 1st report. Bull. JSME 24, 323–331. https://doi.org/10.1299/jsme1958.24.323.
Ishigai, S., Nishikawa, E., Nishimura, K., Cho, K., 1972. Experimental study on structure of gas flow in tube banks with tube axes normal to flow: part 1, Karman Vortex flow from two tubes at various spacings. Bull. JSME 15, 949–956. https://doi.org/10.1299/jsme1958.15.949.
Jung, J., Kuo, C.-J., Peles, Y., Amitay, M., 2012. The flow field around a micropillar confined in a microchannel. Int. J. Heat Fluid Fl. 36, 118–132. https://doi.org/10.1016/j.ijheatfluidflow.2012.04.009.
Kanaris, N., Grigoriadis, D., Kassinos, S., 2011. Three dimensional flow around a circular cylinder confined in a plane channel. Phys. Fluids 23 (6), 064106.
Lee, C.Y., Wang, W.T., Liu, C.C., Fu, L.M., 2016. Passive mixers in microfluidic systems: a review. Chem. Eng. J. 288, 146–160. https://doi.org/10.1016/j.cej.2015.10.122.
Li, J., Chambarel, A., Donneaud, M., Martin, R., 1991. Numerical study of laminar flow past one and two circular cylinders. Comput. Fluids 19, 155–170. https://doi.org/10.1016/0045-7930(91)90031-C.
Li, L., Liu, J., Pan, Z., 2022. Enhancement of heat transfer and mixing with two side-by-side freely rotatable cylinders in microchannel. Int. J. Heat Mass Transf. 189,. https://doi.org/10.1016/j.ijheatmasstransfer.2022.122717 122717.
Mariotti, A., Galletti, C., Brunazzi, E., Salvetti, M.V., 2019. Steady flow regimes and mixing performance in arrow-shaped micro-mixers. Phys. Rev. Fluids 4,. https://doi.org/10.1103/PhysRevFluids.4.034201 034201.
Mathupriya, P., Chan, L., Hasini, H., Ooi, A., 2018. Numerical study of flow characteristics around confined cylinder using OpenFOAM. Int. J. Eng. Sci. 7, 617.
Mizushima, J., Suehiro, N., 2005. Instability and transition of flow past two tandem circular cylinders. Phys. Fluids 17 (10), 104107.
Olsen, M.G., Adrian, R.J., 2000. Out-of-focus effects on particle image visibility and correlation in microscopic particle image velocimetry. Exp. Fluids 29, S166–S174. https://doi.org/10.1007/s003480070018.
Poelma, C., Kloosterman, A., Hierck, B.P., Westerweel, J., Emmert-Buck, M.R., 2012. Accurate blood flow measurements: are artificial tracers necessary? PLoS One 7 (9), e45247.
Pothos, S., Boomsma, A., Troolin, D., Bhattacharya, S., Vlachos, P., 2016. PIV uncertainty: computational and experimental evaluation of the peak ratio method. In: Presented at the ASME 2016 Fluids Engineering Division Summer Meeting collocated with the ASME 2016 Heat Transfer Summer Conference and the ASME 2016 14th International Conference on Nanochannels, Microchannels, and Minichannels, ASME, Washington, DC, USA, p. V002T10A005. doi: 10.1115/FEDSM2016-7926
Renfer, A., Tiwari, M.K., Brunschwiler, T., Michel, B., Poulikakos, D., 2011. Experimental investigation into vortex structure and pressure drop across microcavities in 3D integrated electronics. Exp. Fluids 51, 731–741. https://doi.org/10.1007/s00348-011-1091-5.
Renfer, A., Tiwari, M.K., Tiwari, R., Alfieri, F., Brunschwiler, T., Michel, B., Poulikakos, D., 2013. Microvortex-enhanced heat transfer in 3D-integrated liquid cooling of electronic chip stacks. Int. J. Heat Mass Transf. 65, 33–43. https://doi.org/10.1016/j.ijheatmasstransfer.2013.05.066.
Roshko, A., 1955. On the wake and drag of bluff bodies. J. Aero. Sci. 22, 124–132. https://doi.org/10.2514/8.3286.
Roshko, A., 1954. On the drag and shedding frequency of two-dimensional bluff bodies. NACA, Washington.
Santana, H.S., Silva, J.L., Taranto, O.P., 2019. Development of microreactors applied on biodiesel synthesis: From experimental investigation to numerical approaches. J. Ind. Eng. Chem. 69, 1–12. https://doi.org/10.1016/j.jiec.2018.09.021.
Sharman, B., Lien, F.S., Davidson, L., Norberg, C., 2005. Numerical predictions of low Reynolds number flows over two tandem circular cylinders. Int. J. Numer. Meth. Fluids 47, 423–447. https://doi.org/10.1002/fld.812.
Soleymani, A., Kolehmainen, E., Turunen, I., 2008. Numerical and experimental investigations of liquid mixing in T-type micromixers. Chem. Eng. J. 135, S219–S228. https://doi.org/10.1016/j.cej.2007.07.048.
Sumner, D., 2010. Two circular cylinders in cross-flow: a review. J. Fluid Struct. 26, 849–899. https://doi.org/10.1016/j.jfluidstructs.2010.07.001.
Sumner, D., Price, S.J., Païdoussis, M.P., 2000. Flow-pattern identification for two staggered circular cylinders in cross-flow. J. Fluid Mech. 411, 263–303. https://doi.org/10.1017/S0022112099008137.
Tasaka, Y., Kon, S., Schouveiler, L., Le Gal, P., 2006. Hysteretic mode exchange in the wake of two circular cylinders in tandem. Phys. Fluids 18 (8), 084104.
Tata Rao, L., Goel, S., Kumar Dubey, S., Javed, A., 2019. Performance investigation of T-shaped micromixer with different obstacles. J. Phys. Conf. Ser. 1276 (1), 012003.
Wang, X.K., Tan, S.K., 2008. Near-wake flow characteristics of a circular cylinder close to a wall. J. Fluid Struct. 24, 605–627. https://doi.org/10.1016/j.jfluidstructs.2007.11.001.
Wang, W., Zhao, S., Shao, T., Jin, Y., Cheng, Y., 2012. Visualization of micro-scale mixing in miscible liquids using μ-LIF technique and drug nano-particle preparation in T-shaped micro-channels. Chem. Eng. J. 192, 252–261. https://doi.org/10.1016/j.cej.2012.03.073.
Wetton, B.T.R., 1992. Finite difference vorticity methods. In: Heywood, J.G., Masuda, K., Rautmann, R., Solonnikov, V.A. (Eds.), The Navier-Stokes Equations II — Theory and Numerical Methods, Lecture Notes in Mathematics. Springer, Berlin, Heidelberg, pp. 210–225. doi: 10.1007/BFb0090344.
Wu, S.-J., Hsu, H.-C., Feng, W.-J., 2014. Novel design and fabrication of a geometrical obstacle-embedded micromixer with notched wall. Jpn. J. Appl. Phys. 53 (9), 097201.
Xu, G., Zhou, Y., 2004. Strouhal numbers in the wake of two inline cylinders. Exp. Fluids 37, 248–256. https://doi.org/10.1007/s00348-004-0808-0.
Yang, A.S., Chuang, F.C., Chen, C.K., Lee, M.H., Chen, S.W., Su, T.L., Yang, Y.C., 2015. A high-performance micromixer using three-dimensional Tesla structures for bio-applications. Chem. Eng. J. 263, 444–451. https://doi.org/10.1016/j.cej.2014.11.034.
Zdravkovich, M.M., 1977. REVIEW—review of flow interference between two circular cylinders in various arrangements. J. Fluid Eng. 99, 618–633. https://doi.org/10.1115/1.3448871.
Zdravkovich, M.M., 1987. The effects of interference between circular cylinders in cross flow. J. Fluid Struct. 1, 239–261. https://doi.org/10.1016/S0889-9746(87)90355-0.
Zhang, S., Cagney, N., Balabani, S., Naveira-Cotta, C.P., Tiwari, M.K., 2019. Probing vortex-shedding at high frequencies in flows past confined microfluidic cylinders using high-speed microscale particle image velocimetry. Phys. Fluids 31 (10), 102001.
Zhang, S., Cagney, N., Lacassagne, T., Balabani, S., Naveira-Cotta, C.P., Tiwari, M.K., 2020. Mixing in flows past confined microfluidic cylinders: effects of pin and fluid interface offsetting. Chem. Eng. J. 397,. https://doi.org/10.1016/j.cej.2020.125358 125358.
Zhao, Y., Shen, A.Q., Haward, S.J., 2016. Flow of wormlike micellar solutions around confined microfluidic cylinders. Soft Matter 12, 8666–8681. https://doi.org/10.1039/C6SM01597B.
Zheng, Z., Chen, Z., Zhang, Z., Xiong, G., Zhu, J., Li, Z., 2021. Simultaneous PM2.5 and moisture removal from wet flue gas by a gas-liquid cross flow array. Process Saf. Environ. Prot. 148, 382–391. https://doi.org/10.1016/j.psep.2020.10.019.
Zhou, Y., Yiu, M.W., 2006. Flow structure, momentum and heat transport in a two-tandem-cylinder wake. J. Fluid Mech. 548, 17. https://doi.org/10.1017/S002211200500738X.